



## Surface tailoring on SrMnO<sub>3</sub>@SmMn<sub>2</sub>O<sub>5</sub> for boosting the performance in diesel oxidation catalyst



Qilei Yang <sup>a,1</sup>, Xiyang Wang <sup>b,1</sup>, Houlin Wang <sup>a</sup>, Xinbo Li <sup>c</sup>, Qi Li <sup>a</sup>, Yimin Wu <sup>b</sup>, Yue Peng <sup>a,\*</sup>, Yongliang Ma <sup>a</sup>, Junhua Li <sup>a</sup>

<sup>a</sup> School of Environment, Tsinghua University, Beijing 100084, PR China

<sup>b</sup> Waterloo Institute for Nanotechnology, University of Waterloo, Waterloo, Ontario N2L 3G1, Canada

<sup>c</sup> College of Chemistry, Jilin University, Changchun 130012, PR China

### ARTICLE INFO

#### Keywords:

DOC  
Mullite  
Perovskite  
NO oxidation  
Selective dissolution

### ABSTRACT

Balance of activity and thermal stability for diesel oxidation catalyst (DOC) is difficult to control in terms of different modification methods. We prepare SrMnO<sub>3</sub>-mixed SmMn<sub>2</sub>O<sub>5</sub> (SMO) by the one-pot calcination, then followed in 5 M HNO<sub>3</sub> treatment to yield Mn<sup>4+</sup>@SMO catalyst. Highly active Mn<sup>4+</sup> cations form on SMO surface as amorphous MnO<sub>2</sub> via removing nearly all the Sr in perovskite framework and surface Sm of SMO. Mn<sup>4+</sup>@SMO exhibits superior DOC performance compared with pristine and MnO<sub>2</sub>-doped SMO under a GHSV of 120000 mL·g<sup>-1</sup>·h<sup>-1</sup> or even after 800 °C hydrothermal aging, since it possesses higher average oxidation state of Mn, more oxygen vacancies, stronger covalent bonds of Mn-O, and larger NO adsorption above 200 °C. DRIFTS, NAP-XPS, and isotopic analysis demonstrate that the exposed Mn<sup>4+</sup> cations are the major sites for nitrate or nitrite adsorptions, while both CO and NO oxidation reactions follow the MvK mechanism.

### 1. Introduction

Diesel engines with high air-to-fuel ratios have attracted significant attentions due to their high fuel efficiency. Governmental regulations concerning on atmospheric pollution from diesel engines are becoming increasingly stringent. Environmental Protection Agency (EPA) signed the US 2010 emission standards for heavy-duty diesels, in which all the on-road heavy-duty diesels require NO<sub>x</sub> exhaust limited to 0.27 g·kW<sup>-1</sup>·h<sup>-1</sup>. In 2019, the California Air Resources Board (CARB) published the ultralow-NO<sub>x</sub> emission standards with lower than 0.02 g·kW<sup>-1</sup>·h<sup>-1</sup> NO<sub>x</sub> over certain cycles, which is a 90% reduction in NO<sub>x</sub> emissions compared to up-to-date Euro VI and Chinese National VI standards. [1,2] Such strict standards enforce us to develop the post-treatment catalysts with more effectiveness and longer running lifetime. Diesel oxidation catalyst (DOC) is usually installed just after the engines but before diesel particulate filters (DPF) to control hydrocarbons (HCs) and CO, and generate NO<sub>2</sub> via NO oxidation for soot removing in DPF. Therefore, the catalyst should possess both good oxidation ability to NO, CO, HCs, and structural stability to thermal impulses from the engine. [3,4].

Besides the traditional Pt-based DOC, complex metal oxides are also comprehensively studied because of their low cost and comparative oxidation activities to noble metals. [5] Specifically, some of the tuned perovskites (ABO<sub>3</sub>) or mullite (AB<sub>2</sub>O<sub>5</sub>) catalysts have been declared to be promising and efficient candidates in DOC. The A-sites are usually occupied by rare-earth (La, Sm) or alkaline-earth (Sr, Ba) to stabilize the entire structure, whereas the B-sites are filled with transition metals (Mn, Co) to present adsorption and redox property. [6,7] One of the optimization strategies is to expose more B-sites on the catalyst surface. Our previous work proposed a selective dissolution (SD) treatment method using acid solutions to etch A-sites of LaMn(Co)O<sub>3</sub> perovskites in CO oxidation or NO<sub>x</sub> storage and reduction reactions. [8–10] The dissolution of La<sub>2</sub>O<sub>3</sub> and disproportionation reaction (2Mn<sup>3+</sup><sub>solid</sub> → Mn<sup>4+</sup><sub>solid</sub> + Mn<sup>2+</sup><sub>liquid</sub>) of Mn<sub>2</sub>O<sub>3</sub> in acid solution made perovskites form MnO<sub>2</sub> on the outermost layer, and finally a like-γ-MnO<sub>2</sub> phase was detected with elevated treatment time. However, the thermal stability of the perovskites was nearly totally lost due to the collapse of its frameworks. [11] Thus, this method could only be used to treat the catalyst in certain scenarios at low temperatures or without any thermal aging.

Pristine SmMn<sub>2</sub>O<sub>5</sub> (SMO) exhibits acceptable NO oxidation activity

\* Corresponding author.

E-mail address: [pengyue83@tsinghua.edu.cn](mailto:pengyue83@tsinghua.edu.cn) (Y. Peng).

<sup>1</sup> The authors contributed equal.

due to its unique Mn-Mn dimers as well as excellent thermal and stream resistance due to its mullite structure in DOC reactions. Surface modification on SMO to expose more redox sites is the reasonable design destination to improve its activity to NO, CO and HCs. [12] As for the SD treatment on SMO, inert Sm sites on SMO surface were etched and more active Mn ( $Mn-Mn/Mn-O$ ) sites exposed on SMO-H. Nevertheless, the SD treatment on SMO shows weak response, since molar ratio of  $Mn^{4+}$  and  $Mn^{3+}$  in SMO is 1, and the original or newly formed surface  $Mn^{4+}$  cations inhibit the further etching process. The end effect is that thin  $MnO_2$  from perovskite precipitates on the outermost of SMO surface, similar as coating a layer of active component on thermally stable support. This synergistic effects of  $Mn^{4+}$  cations on the SMO-H catalyst were beneficial to the improvement of  $NH_3$ -SCR performance. [13,14] Therefore, to expand the applied range of the SD method, Shan et al. group reported an amorphous  $MnO_x/SmMn_2O_x$  catalyst prepared by SD treatment via A-site cation exfoliation of  $SmMn_2O_x$ . [15] The robust connection between amorphous  $SmMn_2O_x$  and  $MnO_x$  accelerated the propane catalytic activity. The reconstructed  $MnO_x$  were mostly composed of  $Mn_2O_3$ . The high valence Mn was more favorable to the improvement of DOC oxidation performance. Meanwhile, exposure of  $Mn^{4+}$  on the mullite surface was also beneficial to the improvement of sulfur resistance, mainly due to the increases in acidity of surface  $Mn^{4+}$  cations, weakening the interaction with  $SO_2$ . [16].

To better design the perovskite precursor on mullite, Sr was chosen as the structure promoter. Because of Sr is easier to be tuned by partial substitution of A-site cations in composite metal oxides mullite and form  $SrMnO_3$  perovskite in-situ. This modification also leads to the generation of surface defects and variable oxidation states of B-site elements, therefore, addition of Sr increases the surface area, exposing more active sites, which indicated that dopant Sr provides the number of adsorption sites. [12] Meanwhile,  $SrMnO_3/SMO$  ( $17.41\text{ m}^2\text{ g}^{-1}$ ) possesses a larger specific surface area compared with the raw SMO ( $11.39\text{ m}^2\text{ g}^{-1}$ ) as list in Table S1.

In this work,  $SrMnO_3$ -mixed  $SmMn_2O_5$  was first prepared by a one-pot non-stoichiometric synthesis process. [17] Then, the catalyst was treated using the SD method to obtain  $Mn^{4+}@SMO$ , which amorphous  $MnO_2$  formed by removing Sr in  $SrMnO_3$  perovskites and SMO surface Sm cations are partially removed with the exposure of more  $Mn^{4+}$ . This modification also increased the surface defects and oxidation states of B-sites.

## 2. Experimental section

### 2.1. Catalysts preparation

$SrMnO_3/SmMn_2O_5$  ( $SrMnO_3/SMO$ ) was prepared according to a sol-gel method.  $Sm(NO_3)_3 \cdot 0.6 H_2O$ ,  $Sr(NO_3)_2$  and  $Mn(NO_3)_3 \cdot 0.9 H_2O$  were dissolved in deionized water with certain molar ratio of Sm: Sr: Mn (0.8: 0.2: 2). The resultant solution was dried at  $80^\circ C$  for 12 h and calcined at  $800^\circ C$  for 8 h.  $SrMnO_3/SMO-2$ ,  $SrMnO_3/SMO-10$  and  $Mn^{4+}@SMO$  (1 g) were prepared by the SD treatment method in 5 M  $HNO_3$  (100 mL) for 2 min, 10 min and 10 h, respectively. Then, the mixtures were washed, dried at  $80^\circ C$  for 12 h and calcined at  $800^\circ C$  for 8 h. The operated  $Mn^{4+}@SMO$  after 50 h test was denoted as  $Mn^{4+}@SMO-50\text{ h}$ , and the operated  $Mn^{4+}@SMO$  after three tests was denoted as  $Mn^{4+}@SMO-3\text{ C}$ . The aged  $Mn^{4+}@SMO$  at  $800^\circ C$  for 12 h was denoted as  $Mn^{4+}@SMO-800$ . As a comparison,  $MnO_2-SMO$  (imp) was prepared by the impregnation method. [18].

### 2.2. Catalytic performance

The DOC performance was evaluated in a fixed-bed microreactor ( $\Phi = 10.0\text{ mm}$ ) with 0.10 g catalyst (40–60 mesh). The reactant concentrations were 500 ppm NO, 10,000 ppm CO, 2000 ppm  $C_3H_6$ , 10%  $O_2$ , 5 ± 1% water vapor, and balance  $N_2$ . The gas hourly space velocity (GHSV) was  $120,000\text{ mL}\cdot\text{g}^{-1}\cdot\text{h}^{-1}$  and the total flow was  $200\text{ mL}\cdot\text{min}^{-1}$ .

The concentrations of the reactants and products were monitored online by the Gasmet (DX4000) gas analyzer. The detailed descriptions of the NO or CO or  $C_3H_6$  conversion ( $X_{NO}$  or  $CO$  or  $C_3H_6$ , %) and the normalized initial reaction rate ( $r$ ,  $\text{mol}\cdot\text{m}^{-2}\cdot\text{s}^{-1}$ ) are presented in the Section 2 of Supporting Information (SI).

### 2.3. Catalyst characterization

The structural characterizations of the catalysts were determined using XRD, BET, Raman, HRTEM and ICP-OES. The surface compositions were performed by XPS, EDS, soft XAS, EXAFS and EPR. The redox properties were performed by the temperature-programmed studies. The reaction mechanism was tested by NAP-XPS, DRIFTS and isotopic analysis. The detailed characterization descriptions are presented in the Section 2 of SI.

## 3. Results and discussion

### 3.1. DOC performance

Fig. 1a-c shows the conversions of  $Mn^{4+}@SMO$ ,  $MnO_2-SMO$  (imp) and SMO in terms of NO, CO, and  $C_3H_6$  oxidations under wet conditions.  $Mn^{4+}@SMO$  exhibits the highest activity compared with  $MnO_2-SMO$  (imp) and SMO. The sequence of  $T_{80}$  (certain temperature when the conversion is 80%) in NO oxidation is  $Mn^{4+}@SMO < SMO < MnO_2-SMO$  (imp). The sequences of  $T_{100}$  in CO and  $C_3H_6$  oxidations are  $Mn^{4+}@SMO < SMO < MnO_2-SMO$  (imp) and  $Mn^{4+}@SMO < SMO \sim MnO_2-SMO$  (imp). Moreover, the activity of  $MnO_2-SMO$  (imp) is even significantly lower than that of SMO in CO oxidation, indicating that  $MnO_2$  impregnation is less active due to the lack of synergistic effect between  $MnO_2$  and SMO, though BET surface areas are similar ( $11.39\text{ m}^2\text{ g}^{-1}$  VS.  $11.26\text{ m}^2\text{ g}^{-1}$  in Table S1). Fig. 1d shows the NO, CO, and  $C_3H_6$  conversions of  $Mn^{4+}@SMO$  and SMO under a typical DOC flow.  $Mn^{4+}@SMO$  still exhibits better DOC performance than SMO and commercial Pt/Al catalyst (Fig. S2c). The CO and  $C_3H_6$  complete oxidation of  $Mn^{4+}@SMO$  at  $240^\circ C$ , which is higher than that of SMO ( $350^\circ C$ ).

To avoid the influence of specific surface areas,  $Mn^{4+}@SMO$  and SMO catalysts for NO oxidation were employed at comparable reaction condition and the normalized initial reaction rates ( $r$ ,  $\text{mol}\cdot\text{m}^{-2}\cdot\text{s}^{-1}$ ) were calculated are shown in Table S2,  $Mn^{4+}@SMO$  has superior performance to that pristine SMO mullite, suggesting that the improvement of NO oxidation performance is due to the increase of active sites rather than that of surface area.

We have also compared DOC performance and stability (Fig. S1) of  $Mn^{4+}@SMO$  with the other samples. The initial and third tested activities of  $Mn^{4+}@SMO$  are still excellent. The XRD patterns of the catalysts before and after the stability test ( $Mn^{4+}@SMO-3\text{ C}$  and  $Mn^{4+}@SMO-50\text{ h}$ ) are similar (Fig. S2a), indicating bulk phase of the catalysts are quite stable under  $400^\circ C$ . As shown in Fig. S2b and S2c, the activity of  $Mn^{4+}@SMO-800$  is slightly lower than that of  $Mn^{4+}@SMO$  in NO and DOC oxidation, which could be attributed to inevitable phase transfer from  $MnO_2$  to  $Mn_2O_3$  above  $500^\circ C$ . TEM results (Fig. S2d) can also prove the above conclusion, and  $MnO_2$  on the  $Mn^{4+}@SMO-800$  catalyst surface is converted to  $Mn_2O_3$  nanoparticles by hydrothermal aging at  $800^\circ C$ . However, the DOC and NO oxidation performance of  $Mn^{4+}@SMO-800$  are still higher than those of SMO and commercial DOC catalyst (Pt/Al), which indicates that the NO oxidation performance of SMO mullite is mainly related to the Mn content on the catalyst surface. This is also consistent with the conclusion of NAP-XPS that Mn is the main catalytic active sites in SMO mullite. [14].

### 3.2. Bulk phase and surface morphology

The synthesis route of  $Mn^{4+}@SMO$  is shown in Fig. 2a. Nearly all the Sr from  $SrMnO_3$  perovskite and surface Sm from SMO mullite are removed by the SD method, and  $Mn^{4+}$  cations during disproportionation

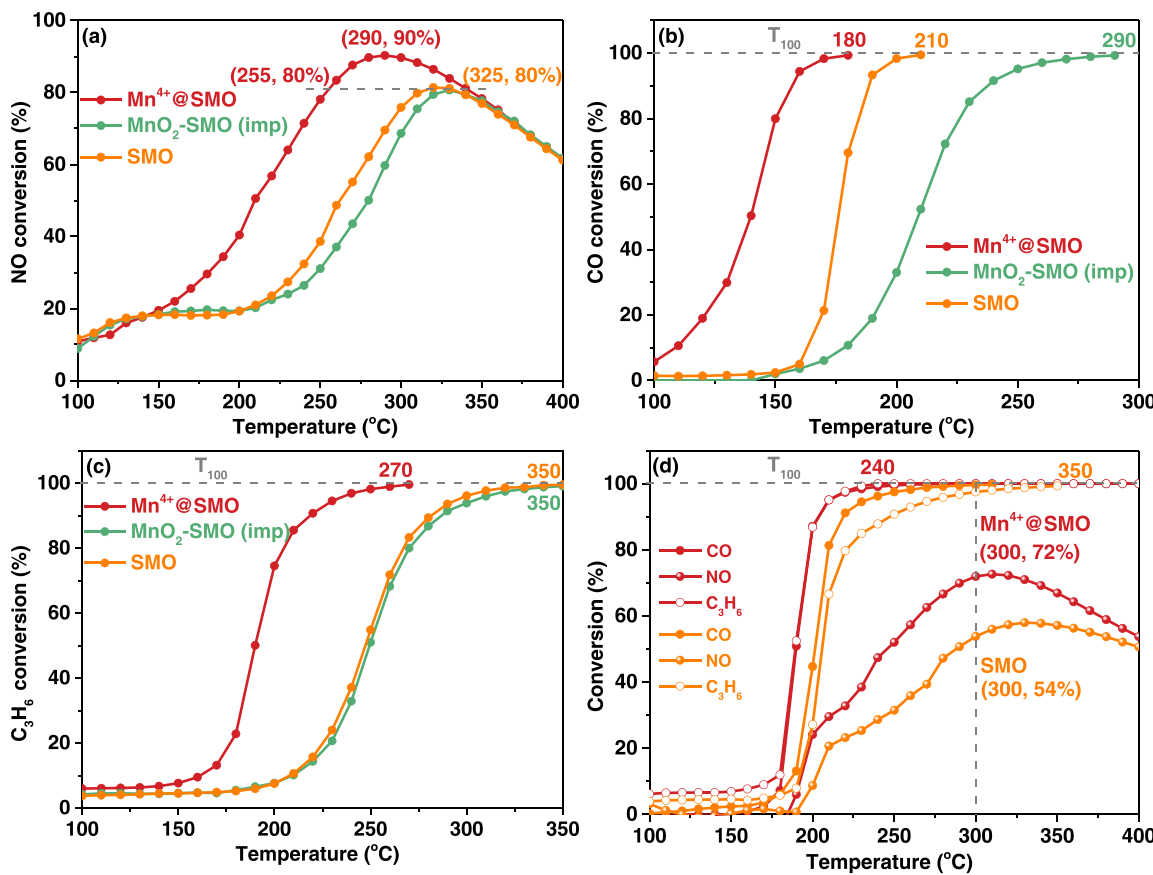


**Fig. 1.** (a) NO, (b) CO and (c) C<sub>3</sub>H<sub>6</sub> conversions of Mn<sup>4+</sup>@SMO, MnO<sub>2</sub>-SMO (imp) and SMO; (d) The DOC performance of Mn<sup>4+</sup>@SMO and SMO.

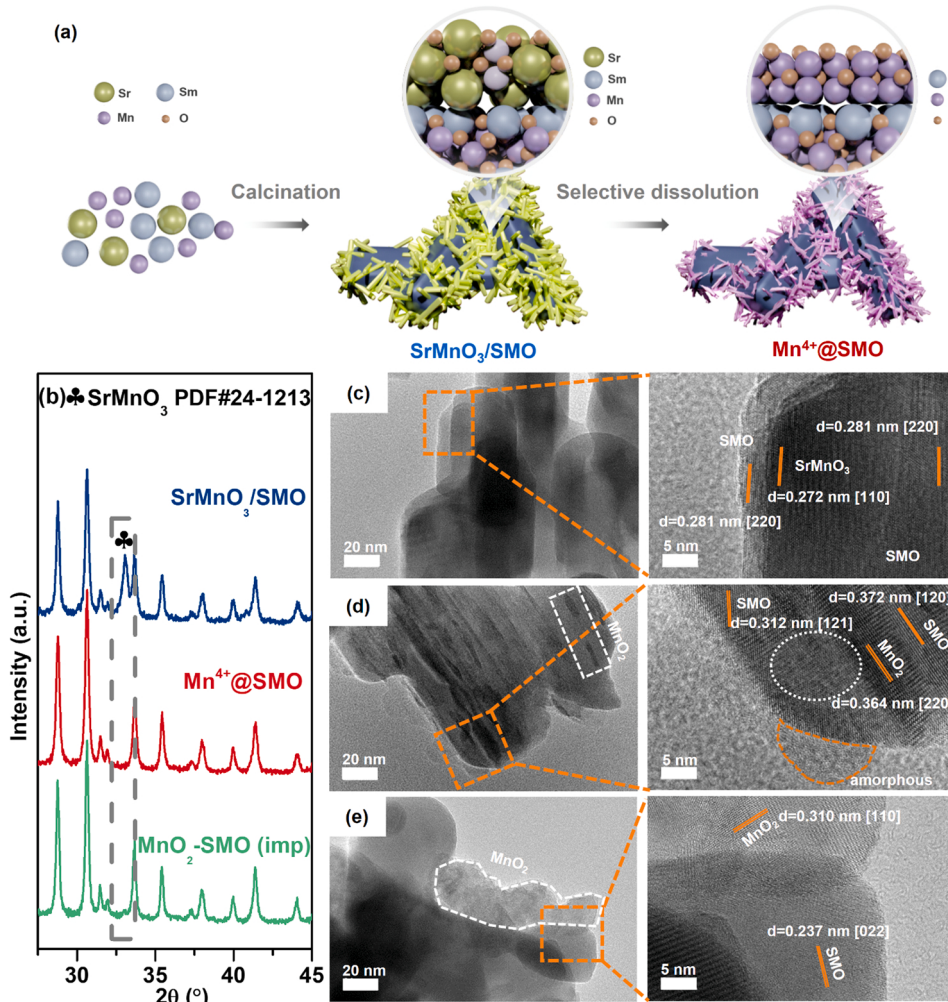
reaction of perovskites directly anchor on SMO surface. Fig. 2b shows the XRD patterns of SrMnO<sub>3</sub>/SMO, Mn<sup>4+</sup>@SMO and MnO<sub>2</sub>-SMO (imp). The mullite phases (JPCDS PDF#52-1096) are well crystallized over SrMnO<sub>3</sub>/SMO, and weak peaks attributed to SrMnO<sub>3</sub> perovskite phases (JPCDS PDF#24-1213) are observed. After the SD treatment, peaks corresponding to SrMnO<sub>3</sub> phases disappeared and Mn<sup>4+</sup>@SMO exhibits pure mullite structure, suggesting the surface MnO<sub>2</sub> could be served as amorphous phase. The XRD patterns of SrMnO<sub>3</sub>/SMO treated with different time are also obtained (Fig. S3), and the patterns show that mullite structure is stable more than 10 h in acid solution. For MnO<sub>2</sub>-SMO (imp), peaks of MnO<sub>2</sub> are not detect, suggesting that impregnated MnO<sub>2</sub> on SMO is also amorphous or uniform.

Fig. 2c-e shows the TEM images of SrMnO<sub>3</sub>/SMO, Mn<sup>4+</sup>@SMO and MnO<sub>2</sub>-SMO (imp), respectively. SrMnO<sub>3</sub>/SMO possesses good crystals. The 0.281 nm *d* spacing is attributed to the [220] crystal plane of SMO and the 0.272 nm *d* spacing is attributed to the [110] crystal plane of SrMnO<sub>3</sub>, respectively. [16] Nonetheless, the surface of Mn<sup>4+</sup>@SMO is quite uneven. The rod-shaped structures of MnO<sub>2</sub> can be seen on the edge and strip-shaped morphology. Mn<sup>4+</sup>@SMO has the lattice spacings (*d* = 0.312 nm and *d* = 0.372 nm) corresponding to the [121] and [120] planes of SMO, and the lattice spacing (*d* = 0.364 nm) corresponding to the [220] planes of MnO<sub>2</sub>. Meanwhile, considerable amount of lattice fringe distortions (highlighted by the white oval) is observed on Mn<sup>4+</sup>@SMO image. It is worth noting that lots of point defects on Mn<sup>4+</sup>@SMO could obscure the distorted lattice fringes. [19,20] However, MnO<sub>2</sub> is agglomerated around the SMO surface in an amorphous form in MnO<sub>2</sub>-SMO (imp), rather than embedded on the SMO surface like Mn<sup>4+</sup>@SMO. EDS mapping is employed to investigate the surface compositions and element distributions (Fig. S4). The elements (Sm, Mn and O) of SrMnO<sub>3</sub>/SMO are uniformly with Sr aggregation on the surface. As for Mn<sup>4+</sup>@SMO, a strong signal for Mn with overlapping

distribution of Mn and Sm are observed, and Sr almost disappears, indicating that the generated Mn<sup>4+</sup> uniformly formed on SMO. In comparison, the distribution of Mn and Sm do not overlap on MnO<sub>2</sub>-SMO (imp). According to the previous research results, NO can be preferably activated on the Mn-Mn dimer sites, SMO mullite with rich oxygen vacancies as well as robust connection between MnO<sub>2</sub> and SMO support, which can accelerate the decomposition of intermediate species in reactants and exhibit the best catalytic oxidation. [15,16] Therefore, the bifunctional active sites exposed on the Mn<sup>4+</sup>@SMO catalyst are more favourable for the synergistic effect of DOC.

The BET surface areas, pore volume and pore diameter of the catalysts are listed in Table S1. The pore diameter of Mn<sup>4+</sup>@SMO (38.77 nm) decreases considerably compared to SrMnO<sub>3</sub>/SMO (63.21 nm), meanwhile, Mn<sup>4+</sup>@SMO (27.71 m<sup>2</sup>·g<sup>-1</sup>) possesses a larger specific surface area than SrMnO<sub>3</sub>/SMO (17.41 m<sup>2</sup>·g<sup>-1</sup>). The elements composition of SrMnO<sub>3</sub>/SMO and Mn<sup>4+</sup>@SMO calculated by the results of XPS, EDS and ICP are summarized in Table S3. The surface ratio of Sm/Mn on SrMnO<sub>3</sub>/SMO is 0.30, which is lower than its theoretical value (0.4) and bulk value (0.45), but the surface of Sr/Mn is 0.19, which is higher than its theoretical value (0.1). The results suggest that the highest exposure of Sr in SrMnO<sub>3</sub>/SMO is due to the preliminary perovskite phase. The surface ratios of Sm/Mn, Sr/Mn and Sr/Sm decrease up to 0.22, 0.01 and 0.07 after the SD treatment, indicating an increase in Mn loading and a decrease in Sr and Sm loadings. Based on the results above, the order of elements solubility in HNO<sub>3</sub> solution is: Sr > Sm > Mn. Therefore, A-sites such as Sr and Sm are more soluble than Mn.

The average valence of Mn on the catalyst is detected by Raman spectra (Fig. S5), since the strong Raman shifts of two phonon peaks at 612 cm<sup>-1</sup> (denoted as  $\alpha$ ) and 675 cm<sup>-1</sup> (denoted as  $\beta$ ) can be attributed to Mn-O stretching vibration of Mn<sup>4+</sup>O<sub>6</sub> octahedron in mullite structures



**Fig. 2.** (a) Synthesis route of the  $\text{Mn}^{4+}$ @SMO catalyst; (b) XRD spectra of  $\text{SrMnO}_3/\text{SMO}$ ,  $\text{Mn}^{4+}$ @SMO, and  $\text{MnO}_2$ -SMO (imp); TEM and HRTEM images of (c)  $\text{SrMnO}_3/\text{SMO}$ , (d)  $\text{Mn}^{4+}$ @SMO and (e)  $\text{MnO}_2$ -SMO.

and symmetric stretching vibration of  $\text{Mn}_2\text{O}_3$ , respectively. [21–23] The normalized peak intensities at  $612 \text{ cm}^{-1}$  and  $675 \text{ cm}^{-1}$  are 1.02 and 0.71 over  $\text{Mn}^{4+}$ @SMO and  $\text{SrMnO}_3/\text{SMO}$ , respectively. The proportion of  $\text{Mn}^{4+}\text{O}_6$  octahedron in  $\text{Mn}^{4+}$ @SMO are 1.44 times higher after the SD treatment, suggesting that more  $\text{Mn}^{4+}$  cations form. [24].

### 3.3. Mn valence and redox property

The XPS spectra of Mn 3 s of the catalysts are shown in Fig. 3a. Empirically, the multiple energy ( $\Delta E$ ) is directly related to its average oxidation state (AOS). The AOS can be calculated by the formula of  $\text{AOS} = 9.27 - 1.18 * \Delta E$ , [25] and the results are listed in Table S3.  $\Delta E$  value of standard  $\text{MnO}_2$  ( $\text{Mn}^{4+}$ ) is 4.70 eV, and the calculated AOS is 3.72. [26]  $\text{Mn}^{4+}$ @SMO (3.55) exhibits similar AOS as  $\text{MnO}_2$ -SMO (imp) (3.50). However, considering their diversity activity profiles, the surface electronic structure and defects play important role in their DOC performance.

The soft XAS absorption spectra of O K-edge (Fig. 3b) and Mn L-edge (Fig. 3c) are used to understand the covalency of Mn and O in different surface-terminated layers. [27, 28] In the O K-edge spectra, peak *a* represents the hybridization of Mn 3d and O 2p orbitals, peak *b* represents the covalent of Mn 3d t<sub>2g</sub>, eg, and O 2p, peaks *c*, *d*, *e* represent the hybridization of O 2p and Sm 5d orbitals, Mn 4s orbitals, and Mn 4p orbitals, respectively, and peak *f* stands for the adsorption oxygen species. [27] Compared with SMO, the white line peaks of  $\text{Mn}^{4+}$ @SMO and  $\text{MnO}_2$ -SMO (imp) present a significant increase in the absorption spectra

of O K-edge and Mn L-edge, suggesting that Mn-terminated catalysts ( $\text{Mn}^{4+}$ @SMO and  $\text{MnO}_2$ -SMO (imp)) have stronger Mn-O covalency and higher valence state of Mn than SMO. The order of surface Mn valence is also consistent with the XPS results. Furthermore, the white peak positions of the Mn L-edge spectra over the three catalysts do not show noticeable change, indicating that the chemical environment of bulk Mn in the catalysts is similar. [28].

The XPS spectra of Mn 2p of the catalysts are shown in Fig. S6. The binding energy of Mn 2p in  $\text{MnO}_2$ -SMO (imp) are 641.7 eV and 653.3 eV, and the binding energy of Mn 2p in  $\text{Mn}^{4+}$ @SMO shifts to slightly higher binding energy (641.9 eV and 653.5 eV). XANES spectra of Mn K-edge and Sm L-edge are shown in Fig. 3d-e. Moreover, the white line peak position and X-ray absorption edge position of Mn on the K-edge of Mn in  $\text{Mn}^{4+}$ @SMO also shifted to higher energy. The results indicate that the average chemical valence of Mn on  $\text{Mn}^{4+}$ @SMO is slightly higher, which shows good accordance with the XPS results of Mn 3 s [29]. On the other hand, the intensity of the white line peak on the Sm L-edge (the valence of Sm) of  $\text{Mn}^{4+}$ @SMO is lower than that of  $\text{MnO}_2$ -SMO (imp), stemming from the significant charge transfer between  $\text{MnO}_2$  and SMO in  $\text{Mn}^{4+}$ @SMO. Fig. 3f shows the Fourier transform function of EXAFS spectra in R-space. Peaks at 1.4 Å, 2.7 Å and 3.6 Å could be assigned to Mn-O, Mn-Mn and Mn-Sm bonds, respectively. [30] As for  $\text{Mn}^{4+}$ @SMO, peaks of Mn-O and Mn-Mn bonds are higher and peak of Mn-Sm bonds slightly lower compared to those of  $\text{MnO}_2$ -SMO (imp). As known, the peak intensity is directly related to the number of the certain bonds in materials. Therefore,  $\text{Mn}^{4+}$ @SMO has

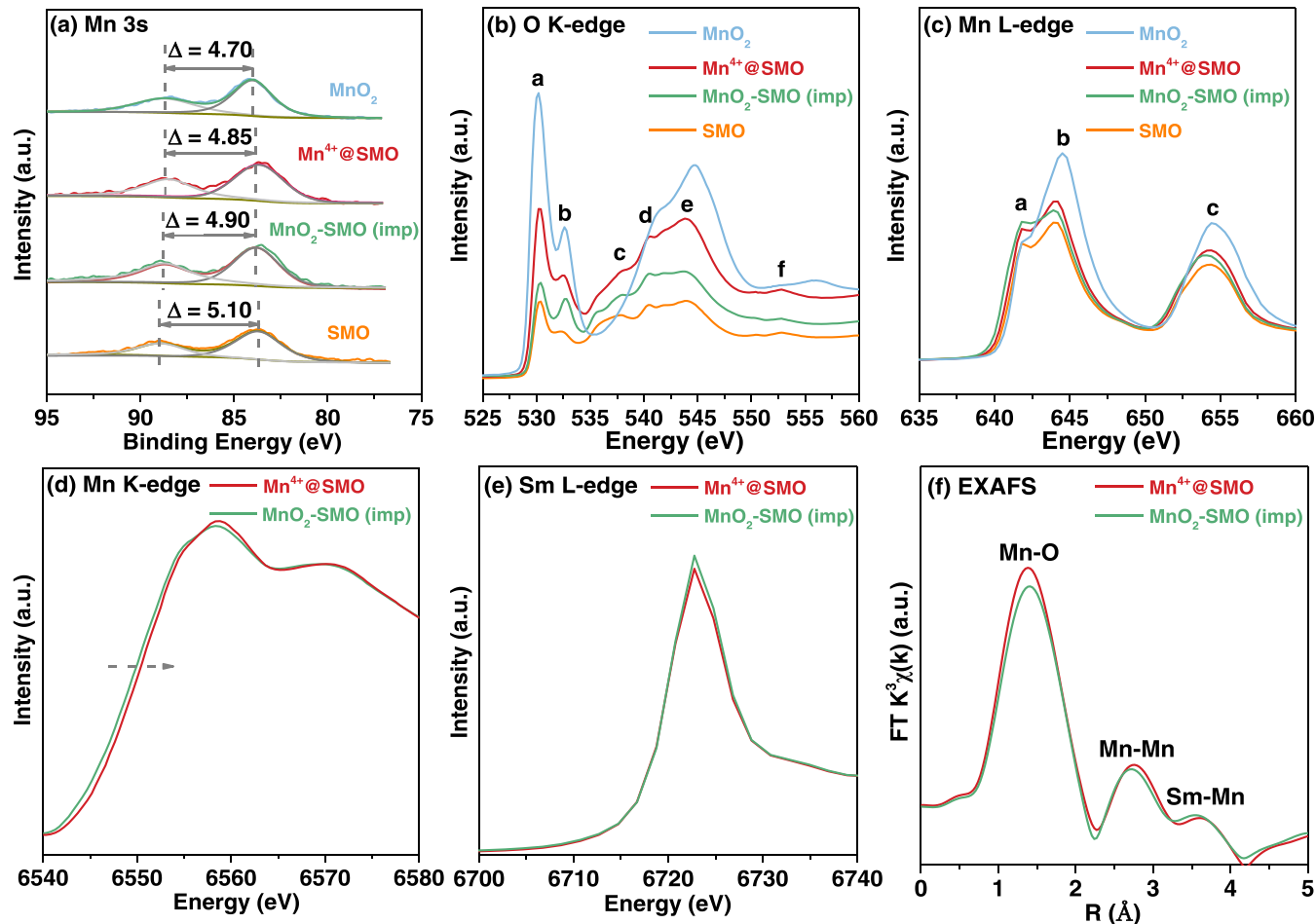


**Fig. 3.** (a) Mn 3 s XPS spectra, (b) O K-edge and (c) Mn L-edge soft X-ray absorption spectra of  $\text{MnO}_2$ ,  $\text{Mn}^{4+}$ @SMO,  $\text{MnO}_2$ -SMO (imp) and SMO; XANES spectra of (d) Mn K-edge, Sm L-edge, and (f) Fourier transforms (FT) ( $k^3\chi(k)$ ) of Mn K-edge extended XAFS oscillation function  $k^3\chi(k)$  in  $\text{Mn}^{4+}$ @SMO and  $\text{MnO}_2$ -SMO (imp).

more Mn-O and Mn-Mn bonds but less Mn-Sm bonds than  $\text{MnO}_2$ -SMO (imp).

$\text{H}_2$ -TPR profiles of the catalysts are shown in Fig. 4a. The peak of SMO at low temperature could be attributed to the surface-adsorbed oxygen and the reduction of  $\text{Mn}^{4+}$  to  $\text{Mn}^{3+}$ , while the peaks at high temperature could be attributed to the reduction of  $\text{Mn}^{3+}$  to  $\text{Mn}^{2+}$ .<sup>[31, 32]</sup> The peak of  $\text{MnO}_2$ -SMO (imp) (438 °C) is higher than that of SMO (418 °C), indicating that  $\text{MnO}_2$ -SMO (imp) is less reducible than SMO. Moreover, there are three reduction peaks for  $\text{Mn}^{4+}$ @SMO. Peak at 214 °C could be attributed to the surface-adsorbed oxygen since those oxygen molecules can be easily dissociated from SMO surface. Peak at 388 °C is lower than SMO (418 °C), indicating that  $\text{Mn}^{4+}$ @SMO is more reducible than SMO due to the enrichment of  $\text{Mn}^{4+}$  on the surface. As listed in Table S4, the quantitative analysis of the  $\text{H}_2$ -TPR was carried out and the total hydrogen consumption of the samples is in the order of  $\text{Mn}^{4+}$ @SMO >  $\text{MnO}_2$ -SMO (imp) > SMO. Compared with SMO,  $\text{MnO}_2$ -SMO (imp) promotes the hydrogen consumption resulting from surface loading of  $\text{MnO}_2$ , i.e.,  $\text{Mn}^{4+}$ @SMO possess higher Mn content and surface oxygen species.

$\text{O}_2$ -TPD profiles of the catalysts are shown in Fig. 4b. Two large peaks are obviously observed at 314 °C and 490 °C in  $\text{Mn}^{4+}$ @SMO. The lower temperature desorption peak could be due to the surface lattice oxygen.<sup>[33]</sup> The quantitative analysis of the  $\text{O}_2$ -TPD was carried out and is shown in Table S4, the order of the oxygen amount per unit gram of samples is  $\text{Mn}^{4+}$ @SMO (0.47 mmol·g<sup>-1</sup>) >  $\text{MnO}_2$ -SMO (imp) (0.28 mmol·g<sup>-1</sup>) > SMO (0.20 mmol·g<sup>-1</sup>). Compared with  $\text{MnO}_2$ -SMO (imp) and SMO,  $\text{Mn}^{4+}$ @SMO possesses significantly more surface adsorbed oxygen species. The number of oxygen vacancies can be

directly measurement by EPR (Fig. 4c), which suggests a signal of oxygen vacancies at g value of 2.003. The signal intensity of oxygen vacancies for  $\text{Mn}^{4+}$ @SMO is 5.75 times higher than the  $\text{MnO}_2$ -SMO (imp). Based on the principle of electroneutrality, since Sr is dissolved by the SD treatment, more  $\text{Mn}^{3+}$  cations are oxidized to  $\text{Mn}^{4+}$  and oxygen vacancies increase on the surface for the adsorption of oxygen species. Therefore, based on the results of  $\text{O}_2$ -TPD and EPR,  $\text{Mn}^{4+}$ @SMO has the largest surface oxygen vacancies. NO-TPD is carried out to investigate NO desorption behaviors (Fig. 4d). The amount of NO capture on  $\text{Mn}^{4+}$ @SMO is greater than that on  $\text{MnO}_2$ -SMO (imp) and SMO in both low (weakly) and high (stable) temperature window. As for  $\text{MnO}_2$ -SMO (imp), it even does not show any NO capacity above 250 °C. The desorption peak at 350 °C of  $\text{Mn}^{4+}$ @SMO is consistent with the peak in  $\text{O}_2$ -TPD, and this peak is directly related to the NO oxidation, i.e., the major capture pathway of NO at high temperature window is via the oxidation with lattice oxygen of catalyst to form nitrate/nitrite species.<sup>[34]</sup>

Combined with the XPS and soft XAS spectra, though  $\text{MnO}_2$ -SMO (imp) displays similar AOS and certain content of  $\text{Mn}^{4+}$  and amorphous  $\text{MnO}_2$  morphology, the lack of synergy effects between  $\text{MnO}_2$  and SMO significantly inhibits its DOC activities compared to  $\text{Mn}^{4+}$ @SMO. The synergy effects of in-situ formed  $\text{Mn}^{4+}$  cations are originated from their higher electronegativity and stronger covalent bonds with lattice oxygen, leading to the formation of more oxygen vacancies for  $\text{O}_2$  activation and  $\text{Mn}^{4+}$  cations for molecules adsorption. Meanwhile, because of the perseverance of SMO structure, the bulk phase of  $\text{Mn}^{4+}$ @SMO does not collapse after the hydrothermal aging at 800 °C.

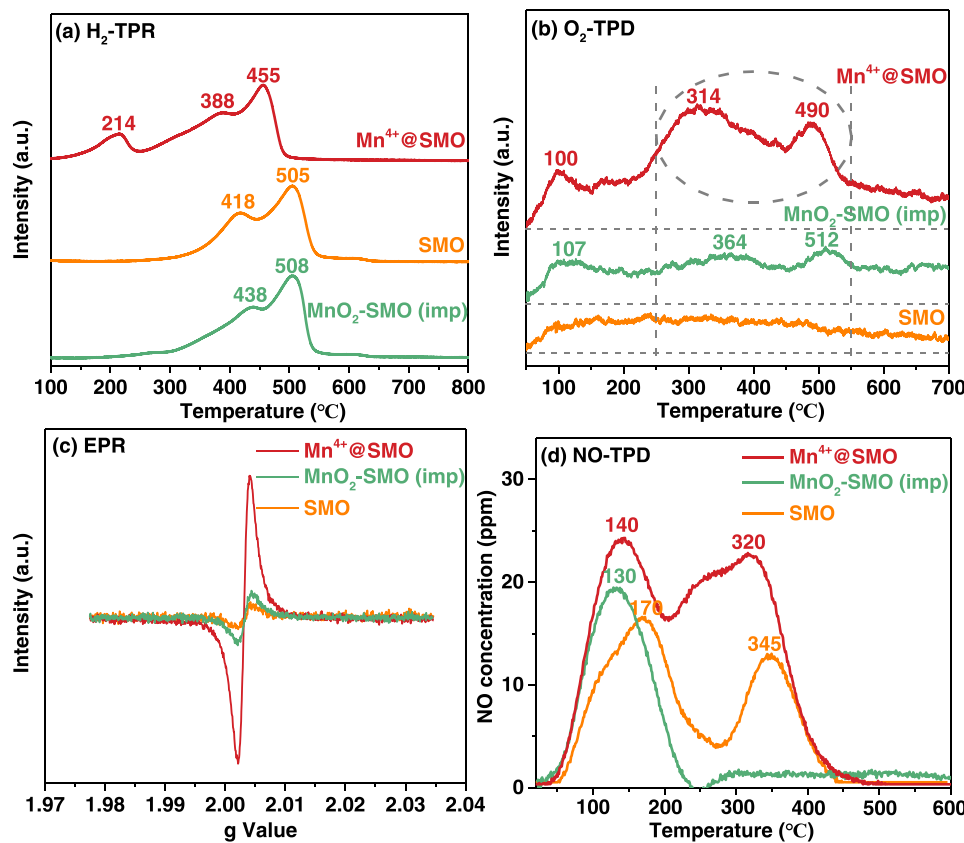


**Fig. 4.** (a) H<sub>2</sub>-TPR, (b) O<sub>2</sub>-TPD, (c) EPR and (d) NO-TPD of Mn<sup>4+</sup>@SMO, MnO<sub>2</sub>-SMO (imp) and SMO.

### 3.4. Catalytic reaction mechanism

Considering the CO and C<sub>3</sub>H<sub>6</sub> oxidation have been systematically studied using in-situ methods and the reaction mechanisms of them are typical the MvK mechanisms without thermodynamics limitations at high temperatures. [35,36] The Eley-Rideal (ER) and Mars-van Krevelen (MvK) mechanisms are the commonly accepted mechanisms of NO oxidation on SMO mullite. [7,37] For ER mechanism, Wang et al. proposed that the NO oxidation mechanism follows the ER mechanism, Mn<sup>4+</sup>-Mn<sup>4+</sup> dimer is the active site, and the desorption of NO<sub>2</sub> on Mn<sup>4+</sup>-Mn<sup>4+</sup> dimer is the rate limiting step. [12] Based on the DFT calculation, Chen et al. proposed that ER and classical MvK mechanism exist simultaneously on mullite surface, and the rate limiting step of NO oxidation is the desorption of NO<sub>2</sub> on Mn-O bond. [38] Zheng et al. proposed that the NO oxidation mechanism follows the synergistic MvK mechanism, and the Mn<sup>3+</sup>-O adjacent Mn<sup>4+</sup>-O<sub>β</sub> sites on the mullite surface play a synergistic role in the catalytic oxidation reaction, NO and O<sub>α</sub> and O<sub>β</sub>. The reaction forms nitrate species adsorbed on the surface. [34] Thampy et al. studied the intermediate products formed by the adsorption of NO on the surface of SMO mullite under different conditions. When lattice oxygen or O<sub>2</sub> is present on the surface of mullite, stable NO<sub>3</sub><sup>-</sup> intermediates will be formed on the surface. [39] Therefore, the NO oxidation mechanism on the surface of SMO mullite may exist ER and MvK mechanisms, and the NO oxidation performance is related to the Mn and oxygen species on the surface of mullite.

Thus, we only compared the difference on the NO oxidation of Mn<sup>4+</sup>@SMO and SMO using in-situ spectra and isotope characterizations. According to our previous work, [14] the exposure of Mn<sup>4+</sup> on SMO surfaces favors the NO oxidation. In-situ NAP-XPS spectra is a powerful tool to detect the valence changes of Sm, Mn, and O during the reactions. Figs. 5a and 5b exhibit the Sm 3d and Mn 2p spectra of Mn<sup>4+</sup>@SMO during NO oxidation, respectively. The binding energy of Sm 3d does not change in both NO and NO + O<sub>2</sub> atmospheres at 25 °C or

250 °C, which is consistent with the conclusion that Sm is not active sites but structure stabilizer on SMO. The binding energy of Mn 2p spectra (641.8 eV) shifts to low binding energy (641.5 eV) in NO with elevated temperature, because NO adsorption on the surface is accompanied by the reduction of Mn<sup>4+</sup>. At 250 °C, when O<sub>2</sub> is introduced into the flue gas, the binding energy shifts of Mn 2p spectra to high binding energy (641.7 eV) due to the promotion of O<sub>2</sub> on NO<sub>2</sub> desorption, and then O<sub>2</sub> recovers the valence state of reduced Mn to fulfil the reaction cycle. Therefore, compared to SMO, Mn<sup>4+</sup>@SMO possesses more Mn<sup>4+</sup> adsorbed sites for NO capture and more vacancies of O<sub>2</sub> adsorbed sites for NO<sub>2</sub> desorption.

Fig. 5c and Fig. S7 show the DRIFTS spectra of Mn<sup>4+</sup>@SMO and SMO at 150 °C for CO adsorption and CO/O<sub>2</sub> co-adsorption, respectively. As a probe molecule, CO is used to study the active sites and possible reaction mechanism. Two peaks at 2175 cm<sup>-1</sup> and 2115 cm<sup>-1</sup> in Fig. 5c represent the absorbed CO on the catalyst. The bands around 1620 cm<sup>-1</sup> and 1430 cm<sup>-1</sup> can be assigned to bicarbonates, whereas bands around 1558 cm<sup>-1</sup> and 1275 cm<sup>-1</sup> can be attributed to the bidentate carbonates. [40] When CO gas is flowed alone, the surface lattice oxygen of Mn<sup>4+</sup>@SMO and SMO can react with the adsorbed CO gas. They exhibit the same intensity in IR signal of CO gas, whereas Mn<sup>4+</sup>@SMO shows higher IR signal of bicarbonates and bidentate carbonates than SMO sample. The result indicates that more lattice oxygen in Mn<sup>4+</sup>@SMO involves in the oxidation of carbon monoxide, which also confirms the improvement of MvK mechanism efficiency. When CO and O<sub>2</sub> are introduced into the flue gas simultaneously, adsorbed CO gas is not observed in IR spectra because CO gas is completely oxidized by oxygen and lattice oxygen. We find that Mn<sup>4+</sup>@SMO exhibit a strong intensity for bicarbonates, while SMO possesses a higher IR signal of bidentate carbonates. Therefore, we can think that CO molecular mainly react with adsorbed oxygen species in SMO catalyst, whereas lattice oxygen of Mn<sup>4+</sup>@SMO involves the CO oxidation reaction.

Furthermore, the in-situ DRIFTS spectra of Mn<sup>4+</sup>@SMO and SMO in

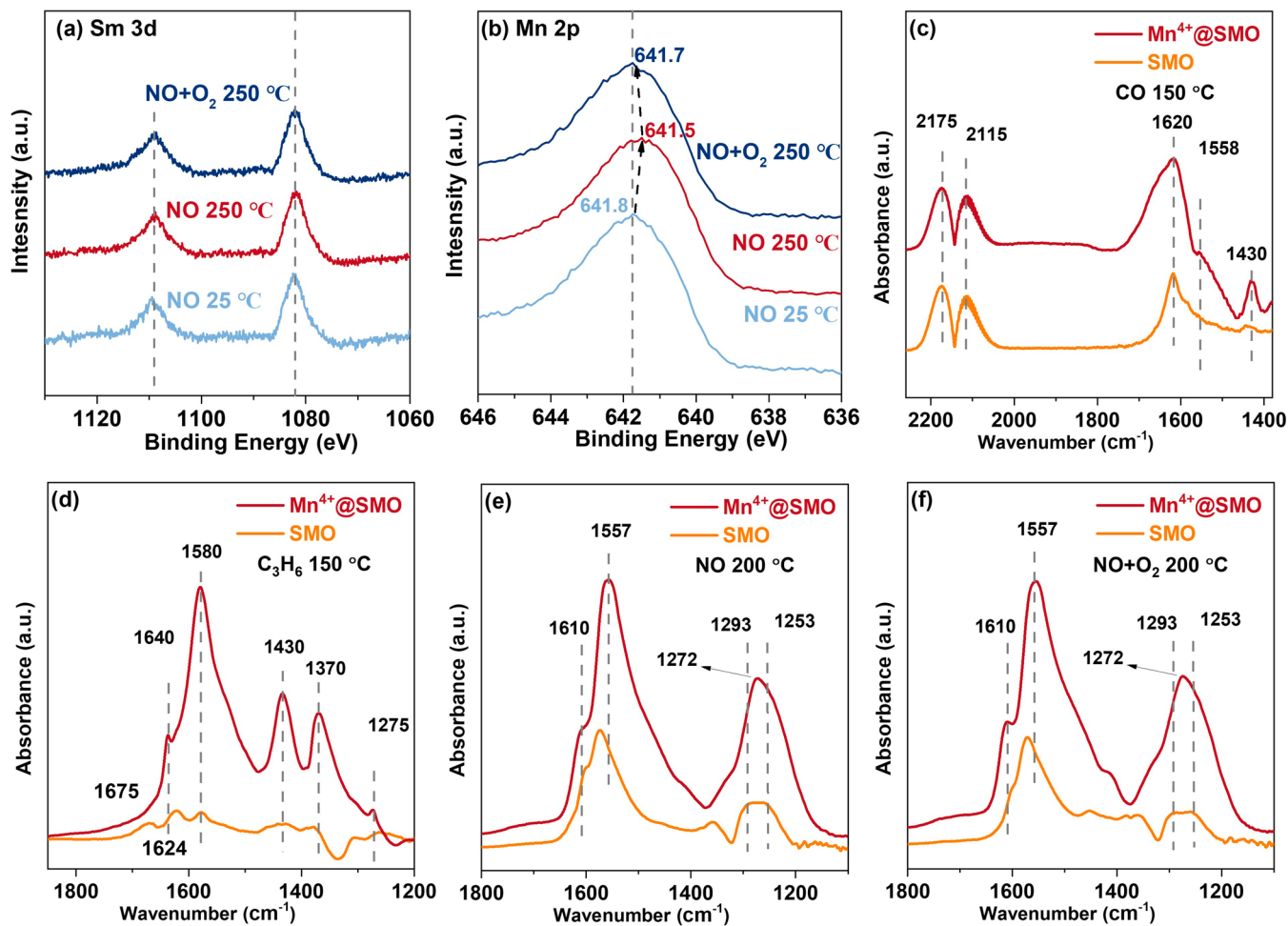


**Fig. 5.** NAP-XPS spectra of (a) Sm 3d and (b) Mn 2p over Mn<sup>4+</sup>@SMO; DRIFTS spectra of (c) CO adsorption at 150 °C, (d) C<sub>3</sub>H<sub>6</sub> adsorption at 150 °C, (e) NO adsorption at 200 °C, (f) NO and O<sub>2</sub> co-adsorption at 200 °C over Mn<sup>4+</sup>@SMO and SMO. (NAP-XPS reaction conditions: The catalyst was sequentially exposed to NO and NO + O<sub>2</sub> at 25 °C and 250 °C. All the Sm 3d and Mn 2p spectra were normalized.).

C<sub>3</sub>H<sub>6</sub> oxidation are measured at 200 °C under the condition of C<sub>3</sub>H<sub>6</sub> and C<sub>3</sub>H<sub>6</sub>/O<sub>2</sub>. Fig. 5d and Fig. S8 that Mn<sup>4+</sup>@SMO has a strong adsorption peak from 3000 cm<sup>-1</sup> to 1200 cm<sup>-1</sup>, where the absorption peaks around 2800–3100 cm<sup>-1</sup> can be assigned as the vibration of C-H groups and the peaks at 1640 cm<sup>-1</sup>, 1580 cm<sup>-1</sup>, 1460 cm<sup>-1</sup>, 1370 cm<sup>-1</sup>, and 1355 cm<sup>-1</sup> are ascribed to the vibration of ν(C=C), ν<sub>as</sub>(COO), ν(COO), ν(C-H), and ν(CO), respectively. Rest bands at 1430 cm<sup>-1</sup>, 1270 cm<sup>-1</sup>, 1672 cm<sup>-1</sup>, and 1310 cm<sup>-1</sup> are considered as ν(CO<sub>3</sub><sup>2-</sup>), ν(C-O), ν(C=O), and ν(HCO<sub>3</sub>), respectively. Mn<sup>4+</sup>@SMO exhibits higher IR signal of ν(C-H), ν(C=C), and ν<sub>as</sub>(COO) than SMO under oxygen free conditions, [13, 39] which indicates that the active surface lattice oxygen in Mn<sup>4+</sup>@SMO facilitate the cleavage of C-H and C-C bonds. When flowing C<sub>3</sub>H<sub>6</sub> and O<sub>2</sub> in the reactor, these signal for ν(C-H), ν(C=C), and ν<sub>as</sub>(COO) in SMO have a remarkable improvement, whereas that of Mn<sup>4+</sup>@SMO have not changed very much. The data confirms that the oxidation of C<sub>3</sub>H<sub>6</sub> in SMO stems from the oxygen atom in oxygen and that in Mn<sup>4+</sup>@SMO can be assigned to the active lattice oxygen. As a result, we can infer that Mn<sup>4+</sup>@SMO mainly comply with MvK reaction mechanism in C<sub>3</sub>H<sub>6</sub> oxidation together with small amount of Langmuir-Hinshelwood (LH) and ER mechanisms, whereas SMO may be dominated by LH and ER mechanisms.

In addition, the DRIFTS spectra of Mn<sup>4+</sup>@SMO and SMO at 200 °C for NO adsorption and NO/O<sub>2</sub> co-adsorption are also collected. As shown in Figs. 5e-5f and Fig. S9, Mn<sup>4+</sup>@SMO has a strong absorption signal of bridged nitrates (~1570 cm<sup>-1</sup> and ~1240 cm<sup>-1</sup>) and monodentate nitrite (~1610 cm<sup>-1</sup> and ~1270 cm<sup>-1</sup>) compared to SMO, [33,

40] which indicates that surface site in Mn<sup>4+</sup>@SMO favors the adsorption and oxidation of NO. Compared to SMO, bridged nitrates around 1570 cm<sup>-1</sup> and 1240 cm<sup>-1</sup> of Mn<sup>4+</sup>@SMO is lower in the ratio of total adsorption species, while monodentate nitrate (1610 cm<sup>-1</sup> and 1270 cm<sup>-1</sup>) is higher. The results indicate that bridged nitrate on Mn<sup>4+</sup>@SMO is converted to monodentate nitrate at 200 °C, and the desorption of monodentate nitrate to NO<sub>2</sub> is the rate-limiting step in NO oxidation. In addition, a peak attributed to nitrate on Sm is observed on SMO (1520 cm<sup>-1</sup>) but it shows quite weak on Mn<sup>4+</sup>@SMO, suggesting that surface exposed Sm could also adsorbed partial NO on SMO, however, it is usually difficult to form NO<sub>2</sub> during the desorption process. [34] When NO gas is flowed alone, the surface lattice oxygen of Mn<sup>4+</sup>@SMO and SMO can react with the adsorbed NO gas and increasing reaction time can enhance the accumulation of nitrate on the surface, which can be considered as MvK mechanism. When NO and O<sub>2</sub> are flowed into the reactor, the reaction time has a weak effect on the adsorbed nitrate species and its signal is lower than that of NO gas (Fig. S9). This result indicates that LH and ER mechanisms also exist in NO oxidation because extra oxygen accelerates the adsorption of nitrate species.

Schematic illustration of the DOC oxidation reaction over the Mn<sup>4+</sup>@SMO catalyst was shown in Fig. 6a. To further compared the reaction mechanism of SMO and Mn<sup>4+</sup>@SMO, <sup>36</sup>O<sub>2</sub> as a tracer is used as a tracer in CO and NO oxidation reactions. The reaction temperatures of CO and NO oxidations are 170 °C and 300 °C, respectively, and the signals of <sup>44</sup>CO<sub>2</sub>, <sup>46</sup>CO<sub>2</sub>, <sup>46</sup>NO<sub>2</sub> and <sup>48</sup>NO<sub>2</sub> are detected using online MS.

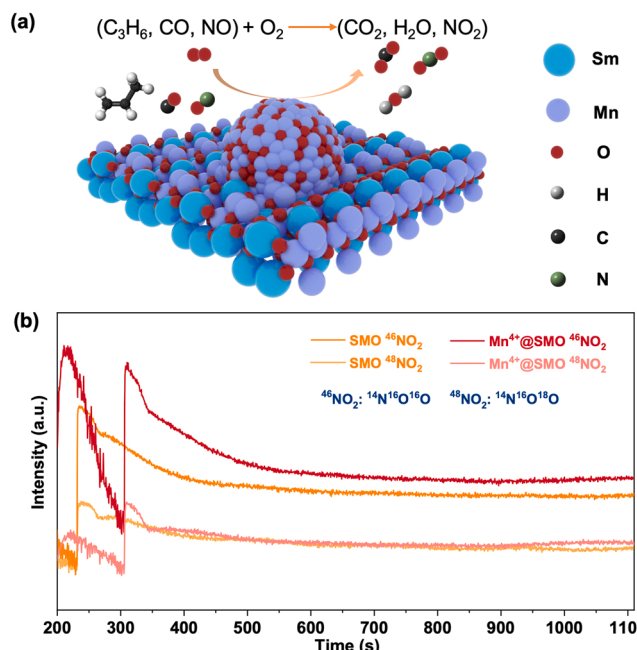


**Fig. 6.** (a) Schematic illustration of the DOC oxidation reaction over the Mn<sup>4+</sup>@SMO catalyst; The isotopic analysis of (b) NO oxidation over Mn<sup>4+</sup>@SMO and SMO. (NO oxidation condition:  $^{36}\text{O}_2$ ,  $\text{N}^{16}\text{O}$ , and lattice  $^{16}\text{O}$  in the catalysts as reactant reagents are converted into  $^{46}\text{NO}_2$  and  $^{48}\text{NO}_2$  during NO oxidation at 300 °C.).

[41] CO oxidation as a model reaction is applied to clarify the surface-active sites and reaction mechanism. As shown in Fig. S10, no signal of  $^{30}\text{CO}$  is detected in CO oxidation, indicating that CO can not readily dissociate into C\* and O\* on the catalyst surface. Signals of  $^{44}\text{CO}_2$  and  $^{46}\text{CO}_2$  are detected on Mn<sup>4+</sup>@SMO and SMO: the signal of  $^{44}\text{CO}_2$  decreases with increasing the reaction time, while the signal of  $^{46}\text{CO}_2$  increases. The signal of  $^{46}\text{CO}_2$  in two catalysts is detectable during the whole experiment. The results indicate that the surface lattice oxygen ( $^{16}\text{O}$ ) is involved in CO oxidation via preliminary the MvK mechanism. The signal of  $^{44}\text{CO}_2$  and  $^{46}\text{CO}_2$  crosses at 670 s and 2180 s on Mn<sup>4+</sup>@SMO and SMO, respectively. The intensity of the signals on Mn<sup>4+</sup>@SMO is stronger than that on SMO, suggesting that Mn<sup>4+</sup>@SMO possess greater exchange capacity of surface oxygen species than SMO, leading to a higher CO oxidation activity at 170 °C. [42] As for NO oxidation (Fig. 6a), the signal of  $^{32}\text{NO}$  does not observe, indicating that NO does not dissociate into N\* and O\* on the catalysts. The signals of  $^{46}\text{NO}_2$  and  $^{48}\text{NO}_2$  are detected in both Mn<sup>4+</sup>@SMO and SMO, the intensity of  $^{48}\text{NO}_2$  tends to be the same. The consistent presence of  $^{46}\text{NO}_2$  on Mn<sup>4+</sup>@SMO and SMO demonstrate that NO oxidation also follows MvK mechanism, i.e., the involvement of surface oxygen species ( $^{16}\text{O}$ ). With increasing reaction time, both catalysts show decrease in  $^{46}\text{NO}_2$  signal, and Mn<sup>4+</sup>@SMO decreases more than SMO. In summary, CO and NO oxidations mainly follow MvK mechanism on Mn<sup>4+</sup>@SMO and SMO, however, higher activity on Mn<sup>4+</sup>@SMO is due to surface oxygen species adsorbed on the abundant vacancies.

#### 4. Conclusion

Therefore, we proposed a novel catalyst design strategy to preserve its oxidation ability and thermal stability simultaneously using the SD treatment method. On the combined interaction of dissolution, disproportionation and redox reactions, surface active Mn<sup>4+</sup> as amorphous MnO<sub>2</sub> formed on SMO surface presents excellent performance compared with the MnO<sub>2</sub>-impregnated or SD-treated SMO counterparts. The tuned surface possesses highly electronegative cations for NO and CO adsorption, and large oxygen vacancies for O<sub>2</sub> decomposition, leading to

the oxidation reactions via MvK mechanism. Whereas, the bulk still displays mullite structure with significantly high resistance to thermal and stream. Considering the relatively simple synthesis route, the catalyst has the potentials for practical use in diesel exhaust control.

#### Associated content

N/A.

#### Supporting information

Detailed characterization techniques, detailed NO, CO, and C<sub>3</sub>H<sub>6</sub> oxidation activity, XRD, EDS, BET, XPS, Raman and ICP results are included.

#### CRediT authorship contribution statement

First author: Qilei Yang, catalysts synthesis, experiments operation and discussion, Xiyang Wang, XAS operation and discussion, Third author: Houlin Wang, TEM operation and DRIFTS spectra operation, Fourth author: Xinbo Li, isotopic analysis operation and discussion, Fifth author: Qi Li, draft revised and results discussion, Sixth author: Yiming Wu, XAS discussion and advises, Corresponding author: Yue Peng, entire experiment design, draft organize and finalized article, Eighth author: Yongliang Ma, proposed the initial research aim, Ninth author: Junhua Li, proposed the initial research aim.

#### Declaration of Competing Interest

The authors declare that they have no known competing financial interests or personal relationships that could have appeared to influence the work reported in this paper.

The authors declare no competing financial interest.

#### Data Availability

Data will be made available on request.

#### Acknowledgment

This work was financially supported by the National Natural Science Foundation of China (22022605) and the Excellence Program of Hefei Science Center, CAS (2020HSC-UE002).

#### Appendix A. Supporting information

Supplementary data associated with this article can be found in the online version at doi:10.1016/j.apcatb.2022.121993.

#### References

- [1] A. Auld, A. Ward, K. Mustafa, Hansen B, Assessment of light duty diesel after-treatment technology targeting beyond euro 6d emissions levels, SAE Int. J. Engines 10 (2017) 1795–1807.
- [2] C. Sharp, C.C. Webb, G. Neely, J.V. Sarlashkar, S.B. Rengarajan, S. Yoon, C. Henry, B. Zavala, Achieving ultra Low NO<sub>x</sub> emissions levels with a 2017 heavy-duty on-highway TC diesel engine and an advanced technology emissions system - NO<sub>x</sub> management strategies, SAE Int. J. Engines 10 (2017) 1736–1748.
- [3] A. Russell, W.S. Epling, Diesel Oxidation Catalysts, Catal. Rev. 53 (2011) 337–423.
- [4] A. Wang, L. Olsson, The impact of automotive catalysis on the United Nations sustainable development goals, Nat. Catal. 2 (2019) 566–570.
- [5] A.K. Datye, M. Votsmeier, Opportunities and challenges in the development of advanced materials for emission control catalysts, Nat. Mater. 20 (2021) 1049–1059.
- [6] Q. Yang, G. Liu, Y. Liu, Perovskite-type oxides as the catalyst precursors for preparing supported metallic nanocatalysts: a review, Ind. Eng. Chem. Res. 57 (2018) 1–17.
- [7] S. Thampy, N. Ashburn, K. Cho, J.W.P. Hsu, Earth-abundant transition metal-based mullite-type oxide catalysts for heterogeneous oxidation reactions, Adv. Energy Sus. Res. 2 (2021), 2000075.

- [8] W. Si, Y. Wang, Y. Peng, J. Li, Selective dissolution of a-site cations in  $\text{ABO}_3$  perovskites: a new path to high-performance, *Catal. Angew. Chem. Int. Ed.* 54 (2015) 7954–7957.
- [9] Y. Peng, W. Si, J. Luo, W. Su, H. Chang, J. Li, J. Hao, J. Crittenden, Surface tuning of  $\text{La}_{0.5}\text{Sr}_{0.5}\text{CoO}_3$  perovskite catalysts by acetic acid for  $\text{NO}_x$  storage and reduction, *Environ. Sci. Technol.* 50 (2016) 6442–6448.
- [10] Y. Peng, W. Si, J. Li, J. Crittenden, J. Hao, Experimental and DFT studies on Sr-doped  $\text{LaMnO}_3$  catalysts for  $\text{NO}_x$  storage and reduction, *Catal. Sci. Technol.* 5 (2015) 2478–2485.
- [11] W. Si, Y. Wang, Y. Peng, X. Li, K. Li, J. Li, A high-efficiency  $\gamma\text{-MnO}_2$ -like catalyst in toluene combustion, *Chem. Commun.* 51 (2015) 14977–14980.
- [12] W. Wang, G. McCool, N. Kapur, G. Yuan, B. Shan, M. Nguyen, U.M. Graham, B. H. Davis, G. Jacobs, K. Cho, X. Hao, Mixed-phase oxide catalyst based on Mn-mullite ( $\text{Sm}, \text{Gd}\text{Mn}_2\text{O}_5$ ) for NO oxidation in diesel exhaust, *Science* 337 (2012) 832–835.
- [13] F. Wang, P. Wang, T. Lan, Y. Shen, W. Ren, D. Zhang, Ultralow-temperature  $\text{NO}_x$  reduction over  $\text{SmMn}_2\text{O}_5$  mullite catalysts via modulating the superficial dual-functional active sites, *ACS Catal.* 12 (2022) 7622–7632.
- [14] Q. Yang, X. Wang, X. Wang, Q. Li, L. Li, W. Yang, X. Chu, H. Liu, J. Men, Y. Peng, Y. Ma, J. Li, Surface reconstruction of a mullite-type catalyst via selective dissolution for NO oxidation, *ACS Catal.* 11 (2021) 14507–14520.
- [15] X. Ma, Y. Tang, Y. Liu, Y. Zhang, L. Jia, X. Liu, C. Du, B. Shan, A-site cation exfoliation of amorphous  $\text{SmMn}_x\text{O}_y$  oxides for low temperature propane oxidation, *J. Catal.* 409 (2022) 59–69.
- [16] W. Yang, J. Gong, X. Wang, Z. Bao, Y. Guo, Z. Wu, A review on the impact of  $\text{SO}_2$  on the oxidation of NO, hydrocarbons, and CO in diesel emission control catalysis, *ACS Catal.* 11 (2021) 12446–12468.
- [17] Q. Yang, Q. Li, X. Wang, X. Wang, L. Li, X. Chu, D. Wang, J. Men, X. Li, W. Si, Y. Peng, Y. Ma, J. Li, Synergistic effects of a  $\text{CeO}_2/\text{SmMn}_2\text{O}_5\text{-H}$  diesel oxidation catalyst induced by acid-selective dissolution drive the catalytic oxidation reaction, *ACS Appl. Mater. Inter.* 14 (2022) 2860–2870.
- [18] L. Long, J. Zhao, L. Yang, M. Fu, J. Wu, B. Huang, D. Ye, Room temperature catalytic ozonation of toluene over  $\text{MnO}_2/\text{Al}_2\text{O}_3$ , *Chin. J. Catal.* 32 (2011) 904–916.
- [19] G. Zhu, J. Zhu, W. Jiang, Z. Zhang, J. Wang, Y. Zhu, Q. Zhang, Surface oxygen vacancy induced  $\alpha\text{-MnO}_2$  nanofiber for highly efficient ozone elimination, *Appl. Catal. B* 209 (2017) 729–737.
- [20] N. Huang, Z. Qu, C. Dong, Y. Qin, X. Duan, Superior performance of  $\alpha@\beta\text{-MnO}_2$  for the toluene oxidation: active interface and oxygen vacancy, *Appl. Catal. A* 560 (2018) 195–205.
- [21] B.J. Rani, G. Ravi, R. Yuvalkumar, S.I. Hong, Novel  $\text{SmMn}_2\text{O}_5$  hollow long nano-cuboids for electrochemical supercapacitor and water splitting applications, *Vacuum* 166 (2019) 279–285.
- [22] W.-R. Wang, G.-X. Song, Y. Zhao, X.-Y. Han, Raman active phonons in  $\text{RMnO}_3$  ( $\text{R}=\text{La, Pr, Nd, Sm}$ ) manganites, *Proc. SPIE* 7282 (2009) 72822R1–72822R4.
- [23] J. Xu, Y.-Q. Deng, Y. Luo, W. Mao, X.-J. Yang, Y.-F. Han, Operando Raman spectroscopy and kinetic study of low-temperature CO oxidation on an  $\alpha\text{-Mn}_2\text{O}_3$  nanocatalyst, *J. Catal.* 300 (2013) 225–234.
- [24] L. Xue, K. Xiong, H. Chen, K. Cho, W. Wang, Investigation of the hydrothermal aging of an Mn-based mullite  $\text{SmMn}_2\text{O}_5$  catalyst of NO oxidation, *RSC Adv.* 7 (2017) 49091–49096.
- [25] Y. Liu, P. Zhang, J. Zhan, L. Liu, Heat treatment of  $\text{MnCO}_3$ : an easy way to obtain efficient and stable  $\text{MnO}_2$  for humid  $\text{O}_3$  decomposition, *Appl. Surf. Sci.* 463 (2019) 374–385.
- [26] M.C. Biesinger, B.P. Payne, A.P. Grosvenor, L.W.M. Lau, A.R. Gerson, R.S.C. Smart, Resolving surface chemical states in XPS analysis of first row transition metals, oxides and hydroxides: Cr, Mn, Fe, Co and Ni, *Appl. Surf. Sci.* 257 (2011) 2717–2730.
- [27] X. Wang, X. Li, X. Chu, R. Cao, J. Qian, Y. Cong, K. Huang, J. Wang, C. Redshaw, R. Sarangi, G. Li, S. Feng, Manipulating surface termination of perovskite manganate for oxygen activation, *Adv. Funct. Mater.* 31 (2021), 2006439.
- [28] X. Long, P. Yu, N. Zhang, C. Li, X. Feng, G. Ren, S. Zheng, J. Fu, F. Cheng, X. Liu, Direct spectroscopy for probing the critical role of partial covalency in oxygen reduction reaction for cobalt-manganese spinel oxides, *Nanomaterials* 9 (2019) 577.
- [29] B.L. Stueben, B. Cantrelle, J. Sneddon, J.N. Beck, Manganese K-edge XANES studies of Mn speciation in Lac des Allemands as a function of depth, *Microchim. J.* 76 (2004) 113–120.
- [30] M.E. Fieser, M.G. Ferrier, J. Su, E. Batista, S.K. Cary, J.W. Engle, W.J. Evans, J. S. Lezama Pacheco, S.A. Kozimor, A.C. Olson, A.J. Ryan, B.W. Stein, G.L. Wagner, D.H. Woen, T. Vitova, P. Yang, Evaluating the electronic structure of formal  $\text{Ln}^{II}$  ions in  $\text{Ln}^{II}(\text{C}_5\text{H}_4\text{SiMe}_3)_3^1$  using XANES spectroscopy and DFT calculations, *Chem. Sci.* 8 (2017) 6076–6091.
- [31] A. Dong, S. Gao, X. Wan, L. Wang, T. Zhang, L. Wang, X. Lang, W. Wang, Labile oxygen promotion of the catalytic oxidation of acetone over a robust ternary Mn-based mullite  $\text{GdMn}_2\text{O}_5$ , *Appl. Catal. B* (2020) 271.
- [32] Z. Feng, J. Wang, X. Liu, Y. Wen, R. Chen, H. Yin, M. Shen, B. Shan, Promotional role of La addition in the NO oxidation performance of a  $\text{SmMn}_2\text{O}_5$  mullite catalyst, *Catal. Sci. Technol.* 6 (2016) 5580–5589.
- [33] S. Thampy, N. Ashburn, C. Liu, K. Xiong, S. Dillon, Y. Zheng, Y.J. Chabal, K. Cho, J. W.P. Hsu, Superior low-temperature NO catalytic performance of  $\text{PrMn}_2\text{O}_5$  over  $\text{SmMn}_2\text{O}_5$  mullite-type catalysts, *Catal. Sci. Technol.* 9 (2019) 2758–2766.
- [34] Y. Zheng, S. Thampy, N. Ashburn, S. Dillon, L. Wang, Y. Jangjou, K. Tan, F. Kong, Y. Nie, M.J. Kim, W.S. Epling, Y.J. Chabal, J.W.P. Hsu, K. Cho, Stable and active oxidation catalysis by cooperative lattice oxygen redox on  $\text{SmMn}_2\text{O}_5$  mullite surface, *J. Am. Chem. Soc.* 141 (2019) 10722–10728.
- [35] J. Hwang, R.R. Rao, L. Giordano, K. Akkiraju, X.R. Wang, E.J. Crumlin, H. Bluhm, Y. Shao-Horn, Regulating oxygen activity of perovskites to promote  $\text{NO}_x$  oxidation and reduction kinetics, *Nat. Catal.* 4 (2021) 663–673.
- [36] L. Nguyen, F.F. Tao, Y. Tang, J. Dou, X.-J. Bao, Understanding catalyst surfaces during catalysis through near ambient pressure X-ray photoelectron spectroscopy, *Chem. Rev.* 119 (2019) 6822–6905.
- [37] J. Yang, J. Zhang, X. Liu, X. Duan, Y. Wen, R. Chen, B. Shan, Origin of the superior activity of surface doped  $\text{SmMn}_2\text{O}_5$  mullites for NO oxidation: a first-principles based microkinetic study, *J. Catal.* 359 (2018) 122–129.
- [38] Z. Chen, X. Liu, K. Cho, R. Chen, B. Shan, Density functional theory study of the oxygen chemistry and NO oxidation mechanism on low-index surfaces of  $\text{SmMn}_2\text{O}_5$  mullite, *ACS Catal.* 5 (2015) 4913–4926.
- [39] S. Thampy, N. Ashburn, S. Dillon, Y. Chabal, K. Cho, J. Hsu, Role of surface oxygen vacancies in intermediate formation on mullite-type oxides upon NO adsorption, *J. Phys. Chem. C* 124 (2022) 15913–15919.
- [40] Y. Wen, C. Zhang, H. He, Y. Yu, Y. Teraoka, Catalytic oxidation of nitrogen monoxide over  $\text{La}_{1-x}\text{Ce}_x\text{CoO}_3$  perovskites, *Catal. Today* 126 (2007) 400–405.
- [41] M. Zeng, X. Wang, Q. Yang, X. Chu, Z. Chen, Z. Li, C. Redshaw, C. Wang, Y. Peng, N. Wang, Y. Zhu, Y.A. Wu, Activating surface lattice oxygen of a  $\text{Cu/Zn}_{1-x}\text{Cu}_x\text{O}$  catalyst through interface interactions for CO oxidation, *ACS Appl. Mater. Inter.* 14 (2022) 9882–9890.
- [42] H. Zhu, Z. Wu, D. Su, G.M. Veith, H. Lu, P. Zhang, S.-H. Chai, S. Dai, Constructing hierarchical interfaces:  $\text{TiO}_2$ -Supported  $\text{PtFe-Fe}_3\text{O}_4$  nanowires for room temperature CO oxidation, *J. Am. Chem. Soc.* 137 (2015) 10156–10159.